Politecnico di Bari

Repository Istituzionale dei Prodotti della Ricerca del Politecnico di Bari

Partially obstructed channel: Contraction ratio effect on the flow hydrodynamic structure and prediction of the transversal mean velocity profile

This is a post print of the following article

Original Citation:
Partially obstructed channel: Contraction ratio effect on the flow hydrodynamic structure and prediction of the transversal mean velocity profile / BEN MEFTAH, M., Mossa, M.. - In: JOURNAL OF HYDROLOGY. - ISSN 0022-1694. - 542:(2016), pp. 87-100. [10.1016/j.jhydrol.2016.08.057]

Availability:
This version is available at http://hdl.handle.net/11589/76234 since: 2021-04-08

Published version
DOI:10.1016/j.jhydrol.2016.08.057

Publisher:

Terms of use:

(Article begins on next page)

17 November 2026

Journal of Hydrology 542 (2016) 87–100

Contents lists available at ScienceDirect

Journal of Hydrology

journal homepage: www.elsevier.com/locate/jhydrol

Research papers

Partially obstructed channel: Contraction ratio effect on the flow hydrodynamic structure and prediction of the transversal mean velocity profile

M. Ben Meftah *, M. Mossa

Department of Civil, Environmental, Building Engineering and Chemistry, Technical University of Bari, Via E. Orabona 4, 70125 Bari, Italy

ARTICLE INFO

Article history:
Received 16 March 2016
Received in revised form 17 June 2016
Accepted 29 August 2016
Available online 30 August 2016
This manuscript was handled by Corrado Corradini, Editor-in-Chief, with the assistance of Subashisa Dutta, Associate Editor

Keywords:
Partially obstructed channels
Emergent vegetation
Contraction ratio
Shear layer
Flow structure
Log-law

ABSTRACT

In this manuscript, we focus on the study of flow structures in a channel partially obstructed by arrays of vertical, rigid, emergent, vegetation/cylinders. Special attention is given to understand the effect of the contraction ratio, defined as the ratio of the obstructed area width to the width of the unobstructed area, on the flow hydrodynamic structures and to analyze the transversal flow velocity profile at the obstructed-unobstructed interface. A large data set of transversal mean flow velocity profiles and turbulence characteristics is reported from experiments carried out in a laboratory flume. The flow velocities and turbulence intensities have been measured with a 3D Acoustic Doppler Velocimeter (ADV)-Vectrino manufactured by Nortek. It was observed that the arrays of emergent vegetation/cylinders strongly affect the flow structures, forming a shear layer immediately next to the obstructed-unobstructed interface, followed by an adjacent free-stream region of full velocity flow.

The experimental results show that the contraction ratio significantly affects the flow hydrodynamic structure. Adaptation of the Prandtl's log-law modified by Nikuradse led to the determination of a characteristic hydrodynamic roughness height to define the array resistance to the flow. Moreover, an improved modified log-law predicting the representative transversal profile of the mean flow velocity, at the obstructed-unobstructed interface, is proposed. The benefit of this modified log-law is its easier practical applicability, i.e., it avoids the measurements of some sensitive turbulence parameters, in addition, the flow hydrodynamic variables forming it are predictable, using the initial hydraulic conditions.

© 2016 Elsevier B.V. All rights reserved.

1. Introduction

Aquatic plants/macrophytes usually play a number of roles on the hydrodynamic behavior and environment dynamic equilibrium of rivers and estuaries, i.e., turbulence, mixing and resistance to the flow (Righetti and Armanini, 2002), flood control, streambed and bank/shoreline stability, water purification, transport and dispersion of nutrients and tracers, protecting and restoring aquatic habitats. Natural vegetation in river floodplains and adjacent wetlands is characterized by multiple aspects (e.g., submerged/emerged, rigid/flexible, leafed/leafless, have branches/rods, high/low density) and can occupy the entire width or a portion of a waterway, reflecting a number of complex phenomena. Therefore, a good knowledge of the physical interaction between a flowing fluid and aquatic vegetation is required to promote best environmental management practice.

Two types of vegetation are usually defined (Järvelä, 2005): stiff/rigid (typically woody or arborescent plants) and flexible (herbaceous plants). Rigid arborescent plants, of random or regular arrays, are widely used as a way of protecting and managing of floodplains and banks (see Fig. 1). Tree farms are also considered as a partially porous obstruction, where fields of trees can be arranged in regular square rows. In addition, flow through rigid and emergent cylinder arrays is commonly found in several engineering application such as offshore structures, transmission lines, chimneys and array of silos. Several of these structures may also show geometries similar to the model geometry investigated in this manuscript. In the present study, we focus on the understanding of the various hydrodynamic phenomena occurring in the interaction between a flowing fluid and these structures.

A number of studies have been carried out towards gaining a better understanding of flow hydrodynamic structure in floodplains and wetlands. Many of these studies were focused on

* Corresponding author.
E-mail addresses: mouldi.benmeftah@poliba.it (M. Ben Meftah), michele.mossa@poliba.it (M. Mossa).

http://dx.doi.org/10.1016/j.jhydrol.2016.08.057
0022-1694/© 2016 Elsevier B.V. All rights reserved.

Nomenclature

a	total frontal area (area exposed to the flow) per unit array (m^{-1})
B	channel width (m)
b	width of the unobstructed area (m)
b_o	width of the obstructed area (m)
C_D	drag coefficient (–)
C_r	contraction ratio (–)
d	cylinder diameter (m)
g	gravity acceleration ($m\ s^{-2}$)
H	flow depth (m)
h	cylinder height (m)
k_s	hydrodynamic roughness height (m)
N	number of velocity sampling (–)
n	density of cylinders (cylinders m^{-2})
Q	channel discharge ($m^3\ s^{-1}$)
Re_0	inlet Reynolds number (–)
Re_2	free-stream Reynolds number (–)
s, s_x, s_y	space between cylinders (m)
T	water temperature (°C)
t	time (s)
U, V	streamwise and spanwise time-averaged velocity ($m\ s^{-1}$)
U_m	streamwise velocity at y_m ($m\ s^{-1}$)
U_0	mean channel velocity upstream of the cylinder arrays ($m\ s^{-1}$)
U_1	flow velocity inside the obstructed region ($m\ s^{-1}$)
U_2	free-stream velocity in the unobstructed area ($m\ s^{-1}$)
U^+, U^{++}	dimensionless streamwise velocities (–)
u^*	friction velocity ($m\ s^{-1}$)
u', v'	longitudinal and transversal velocity fluctuations (ms^{-1})
U'	u'-root mean square ($m\ s^{-1}$)
$U'V'$	spanwise Reynolds stress ($m^2\ s^{-2}$)
x, y, z	longitudinal, transversal and vertical coordinates, respectively (m)
x_{eq}	equilibrium velocity length (m)
y_m	effective shear layer origin (m)
y^+, y^{++}	dimensionless transversal coordinates (–)
α	empirical coefficient (–)
β	empirical constants (–)
δ_2	shear layer width (m)
Φ, C	integration constant (–)
φ	volume solid fraction of the cylinders (–)
κ	von karman's constant (–)
ν	Fluid kinematic viscosity ($m^2\ s^{-1}$)



Fig. 1. Example of floodplains with random and regular arrays of rigid trees.

velocity profiles and turbulent characteristics of partly emergent-vegetated channels (Naot et al., 1996; Nezu and Onitsuka, 2001; Xiaohui and Li, 2002; Helmiö, 2004; White and Nepf, 2007, 2008; Chen et al., 2010; Huai et al., 2011; Ben Meftah et al., 2014; Lima and Izumi, 2014; Wang et al., 2014). Most of these studies are based on laboratory experiments with different artificial roughness (in uniform flow). Experimental results show that the presence of the cylinders/vegetation arrays strongly affects the flow velocity distribution, forming a transversal sharp transition region at the interface between the obstructed and the unobstructed domains. Lima and Izumi (2014) indicated that the presence of partial vegetation/cylinders arrays produces velocity inflection and transverse shear, resulting in a Kelvin-Helmholtz instability with large-scale horizontal vortices centered around the edge of the vegetated area. These vortices have a strong influence on the velocity distribution and enhance the lateral exchange of mass and momentum between the vegetated zone and the open channel (Yang et al., 2015).

White and Nepf (2007, 2008) carried out detailed 2D flow velocity measurements with a Laser Doppler Velocimeter (LDV) in a 1.2 m wide, 13 m long flume, partially obstructed with a 0.4 m wide array of wooden, emergent, circular cylinders of three different volume densities ($\varphi = \pi ad/4 = 0.02$, 0.045 and 0.10), where a is the total frontal area per unit array and d is the cylinder diameter. The authors observed that at the interface between the obstructed and the unobstructed domains, a shear layer is found, possessing two distinct length scales: (i) an inner-layer thickness set by the array resistance, (ii) a wider outer region, which resembles a boundary layer, has a width set by the water depth and bottom friction (see also Ben Meftah et al., 2014). The authors argued that the interfacial Reynolds shear stress approximately balances the array resistance in the sharp transition region across the interface. While, in the boundary layer outside the array, the shear stress approximately balances the pressure gradient from the free-surface slope. According to the authors, as the flow develops the peak of the Reynolds stress shifts toward the interface and becomes more pronounced.

The free shear layer, formed at the interface, is subjected to transversal motion and may be shifted (increase of its width) away from the geometrical edge of the obstructed area (Naot et al., 1996; Ben Meftah et al., 2014). The longitudinal vorticity source, which is attenuated within the obstructed domain, increases externally

leading to an overall increase of the effects of the secondary velocities (Naot et al., 1996). In the unobstructed flow region, flow features resemble those of the boundary layer, whereas in the obstructed region the flow has the features of "porous obstructions" (Hsieh and Shiu, 2006; Huai et al., 2011). According to Vermaas et al. (2011), three mechanisms for exchange of streamwise momentum can be distinguished: cross-channel secondary circulations, turbulent mixing resulting from vortices acting in the horizontal plane, and mass transfer from the decelerating flow in the obstructed flow area to the accelerating flow in the parallel unobstructed area. Following previous studies (e.g., Shiono and Knight, 1991; Van Prooijen et al., 2005), Vermaas et al. (2011) indicated that the contribution of secondary flow to the lateral momentum exchange in compound channels depends very much on the depth of the floodplains relative to the depth of the main channel and on the geometrical details of the interface. Rominger and Nepf (2011) indicated that, upstream of a obstructed area of a finite-width, the flow adjusts over an interior length scale proportional to a drag length scale and the width of the obstructed area, $2b_0$ (full-width of the obstructed area perpendicular to the oncoming flow). Therefore, the three mechanisms for exchange of streamwise momentum indicated above are subject to change on the flow and the vegetation properties, i.e., the mean channel velocity upstream of the vegetation canopy, the vegetation density, the dimensions of both the obstructed and the unobstructed domains. This study aims to establish the effect of the contraction ratio C_r, defined as the ratio of the obstructed area width b_o (Fig. 2) to the width of the unobstructed area b ($C_r = b_o/b$), on the flow structures.

2. Prediction of the mean flow velocity

Numerous methods were recently developed to predict the transverse distributions of the depth averaged velocity for steady uniform flows in partially vegetated rectangular channels. Most of them offer analytical solutions of the transversal mean flow velocity distribution at the interface, based on the double-averaged of Navier-Stokes (N-S) equations (e.g., White and Nepf, 2008; Chen et al., 2010; Ben Meftah et al., 2014; Lima and Izumi, 2014). By assuming that the channel is sufficiently wide (shear layer does not reach the channel wall-sides), outside the shear layer, the transverse velocity vanishes and the streamwise velocity U asymptotically approaches to constant free-stream (slip) velocities U_2. Fig. 2 shows the general problem description of a partly obstructed channel by an array of rigid and emergent vegetation/-cylinders. Fig. 2 indicates the typical shear layer development and the double-averaged (time and space-averaged) transversal profiles of the mean flow velocity $U(y)$ at the interface between the obstructed and the unobstructed domains. In the case where the mean flow depth H is much smaller than the mean channel width, that is $H/B \ll 1$, the flow can be considered, approximately, bi-dimensional (x-y), neglecting the effect of the vertical velocity component (White and Nepf, 2008; Ben Meftah et al., 2014), where x and y respectively indicate the longitudinal and the transversal directions. Some analytical solutions, recently obtained, to predict the typical transversal profile of the mean flow velocity in the unobstructed area are reported in Table 1.

Numerous experimental studies conducted on submerged vegetated channels have shown that the vertical velocity profile above aquatic vegetation follows a logarithmic trend. Therefore, many of these studies adapted the universal logarithmic law of the wall, with specific modifications, to describe this velocity profile (e.g., Järvelä, 2005; Stephan and Gutknecht, 2002). Different methods adapting the vertical velocity profile over aquatic vegetation to the Prandtl's log-law are well summarized in a previous study by Stephan and Gutknecht (2002). At the interface between the obstructed and the unobstructed flow areas of the present study and other previous studies (e.g., Nezu and Onitsuka, 2001; White and Nepf, 2007, 2008; Ben Meftah et al., 2014), independent of the obstructed area characteristics, it is observed that the transversal streamwise velocity almost behaves the same way as a vertical velocity profile above aquatic vegetation, following a logarithmic trend. This similarity between both cases also made us trying to adapt the universal logarithmic law of the wall, to describe the transversal mean velocity profile at the interface in a partly vegetated channel, avoiding the complicated analytical solutions proposed in Table 1. In analogy with the flow velocity distribution above aquatic submerged vegetation, the transversal profile of the mean flow velocity in partly vegetated channel, considering, by analogy, the interface separating both domains as a virtual wall, can be determined as:

$$\frac{U}{u^*} = \frac{1}{\kappa} Ln\left(\frac{y - y_m}{k_s}\right) + C \tag{1}$$

where u^* is the friction velocity, κ is the Von Karman's constant, y_m is determined as the zero plane displacement of the logarithmic

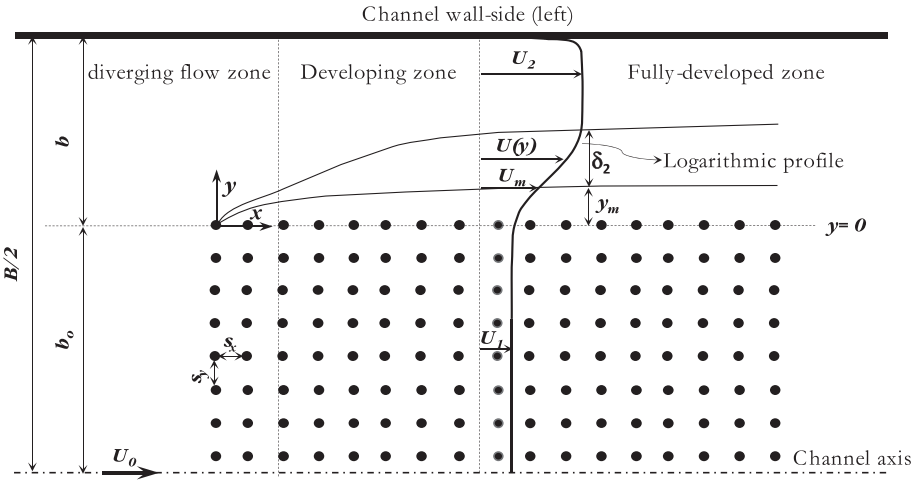


Fig. 2. Problem description at the interface between the obstructed and the unobstructed domains of a partly obstructed channel. B is the channel width, y_m is defined as the effective shear layer origin of δ_2, δ_2 is the shear layer width, U_0 is the mean channel velocity upstream of the obstructed domain, U_m is the streamwise flow velocity at y_m and U_1 is the velocity inside the obstructed region, defined as a time and space-averaged pore velocity.

Table 1
Some analytical solutions, recently obtained, to predict the typical transversal profile of the mean flow velocity in the unobstructed area.

Author	Analytical solution of the mean flow velocity	Notations
White and Nepf (2008)	$\frac{U}{U_2} = 3\tanh^2\left[\sqrt{\frac{3}{4\left(\frac{U_m}{U_2}-2\right)}}\frac{(y-y_m)}{\delta_o}+C\right]-2$	y_m = effective shear layer origin of δ_o; $\delta_o = (U_2-U_m)/\partial U/\partial y\|_{y_m}$ is the shear layer thickness; $C = \tanh^{-1}\sqrt{1+\frac{(U_m/U_2-1)}{3}}$
Chen et al. (2010)	$U(m/s) = \left[\alpha\sqrt{\frac{f_{nv}}{8}}gHS_0(C_3e^{r_3Y}+C_4e^{r_4Y}+\delta_{nv})\right]^{1/2}$	f_{nv} = Darcy-Weisbach friction factor in the unobstracted area; g = gravety acceleration; S_0 = channel slope; C_3 and C_4 are constant to determine; $Y = \frac{y}{B};\ \delta_{nv} = \frac{8}{f_{nv}\sqrt{\frac{f_{nv}}{8}}}$ $r_{3,4} = \frac{K\pm\sqrt{K^2+\frac{f_{nv}}{4}\xi_{nv}\sqrt{\frac{f_{nv}}{8}}}}{\xi_{nv}\sqrt{\frac{f_{nv}}{8}}}\frac{B}{H}$ K = secondary current intensity coefficient; ξ_{nv} = eddy viscosity coefficient
Ben Meftah et al. (2014)	$U^*(y^*) = \frac{1}{2}\left[\left(\frac{\alpha_1}{L}\right)^2+4\frac{\alpha_2}{I}y^*\right]^{\frac{1}{2}}-\frac{\alpha_1}{2L}$ For $0\leqslant y^*<1$ $U^*=1$ For $y^*\geqslant 1$	$U^* = \frac{U-U_m}{U_2-U_m};\ y^* = \frac{y-y_m}{\delta_2};\ H^* = \frac{H}{\delta_2}$ $\alpha_1 = \frac{(L+\frac{I}{2}c_f)U_m+V_m}{U_2-U_m} \approx \frac{LU_m+V_m}{U_2-U_m}$ $\alpha_2 = \frac{gI\delta_2}{(U_2-U_m)^2}$ C_f = bed friction coefficient; I = energy slope; L = secondary current intensity; coefficient $V_m = V(y_m)$ transversal velocity
Lima and Izumi (2014)	$U_0(Y) = 3\tanh^2\left[\left(\frac{\beta}{2\varepsilon}\right)^{1/2}Y+\tanh^{-1}\left(\frac{\psi+2}{3}\right)^{1/2}\right]-2$ for $0\leqslant y\leqslant 1$	$Y = y/b$; $U_0 = U/U_2$; $\beta = \frac{C_f b}{H};\ \varepsilon = \frac{C_f^{1/2}H}{15b}$ In the unobstructed area, $\psi = 1$

profile, k_s is a hydrodynamic roughness height (equivalent sand roughness) and C is the integration constant.

Recently, Ben Meftah and Mossa (2016) tried to find a typical solution predicting the representative transversal profile of the mean flow velocity, at the obstructed-unobstructed interface. Adapting the universal law of the wall, the authors proposed a new modified log-law predicting the transversal velocity distribution in the fully developed zone. The proposed modified log-law contains various empirical constants determined based on the measurement of some sensitive turbulence parameters, i.e., the eddy viscosity and the friction velocity. In addition, the hydrodynamic properties appeared in the modified log-law, i.e., U_2, U_m, y_m and δ_2 are unpredictable, making difficult the practical applicability of this log-law. In this manuscript, we will try, using somewhat different procedure in adapting the universal logarithmic law of the wall, to ovoid the measurement of the sensitive turbulence parameters and to propose empirical formulations to predict the different physical variables composing the log-law.

3. Experimental setup

The experimental runs were carried out in a smooth horizontal very large rectangular channel at the Coastal Engineering Laboratory (L.I.C.) of the Department of Civil, Environmental, Building Engineering and Chemistry at the Technical University of Bari, Italy. The channel consisted of a base and lateral walls made of glass. The channel is 15 m long, 4 m wide and 0.4 m deep. To create a current inside the channel, a closed hydraulic circuit was constructed. The water was pumped, from a large downstream metallic tank, by means a Flygt centrifugal electro-pump to the upstream steel tank. A side-channel spillway with adjustable height made from different plates mounted together was fitted into the upstream tank. The water that overflowed was discharged into the large metallic tank located downstream of the channel. Two different electromagnetic flow meters were mounted onto the hydraulic circuit of the channel, in order to measure both the pumped and the overflowed flow rates. The channel discharge Q was determined as the difference between the two flow rates. To create a smooth flow transition from the upstream tank to the flume, a set of stilling grids were installed in the upstream tank to dampen inlet turbulence. The upstream and downstream gates were used to define the flow depth and mean velocity in the channel (Fig. 3).

The model array is constructed of vertical, rigid, circular and threaded steel cylinders. The cylinder height, h, and diameter are 0.31 m and 0.003 m, respectively. The cylinder extremities are inserted into a plywood plaque 3.0 m long, 4.0 m wide and 0.02 m thick, which in turn is fixed along the channel bottoms, forming the length of the obstructed area. It should be taken into account that the arrays of cylinders are partially mounted on the bottom of the channel, in the central part over a full width of $2b_o$, leaving two symmetric lateral areas, each one of width b, of free flow circulation near the wall-sides. Since a special attention is given to understand the effect of the contraction ratio C_r on the flow structure, experiments were carried out with four different values of C_r, varying b and b_o. The plywood plaque (without array of cylinders) is extended 3 m both upstream and downstream of the experimental area with array of cylinders and is tapered to the channel bottom to minimize flow disturbance. Cylinders were arranged regularly and spaced longitudinally, s_x, and transversally, s_y, with the same distance $s_x = s_y = 5.0$ cm, giving a cylinder density $n = 400$ cylinders/m^2.

The origin of the x-axis ($x = 0$) is taken at the upstream edge of the array of cylinders, while the origin of the y-axis ($y = 0$) is taken at the array edge (interface between the obstructed and unobstructed domains), as shown in Fig. 2. The three flow velocity components were accurately measured using a 3D Acoustic Doppler Velocimeter (ADV)-Vectrino, manufactured by Nortek. The Vectrino was used with a velocity range equal to ±0.30 m/s, a measured velocity accuracy of ±0.5%, a sampling volume of vertical extend of 7 mm, a sampling rate of 150 Hz and a time of acquisition window of 2 min. For high-resolution measurements, the manufacturer recommends a 15 db signal-to-noise ratio (SNR) and a correlation coefficient >70%. The acquired data were filtered based on the Tukey's method and the bad samples (SNR < 15 db

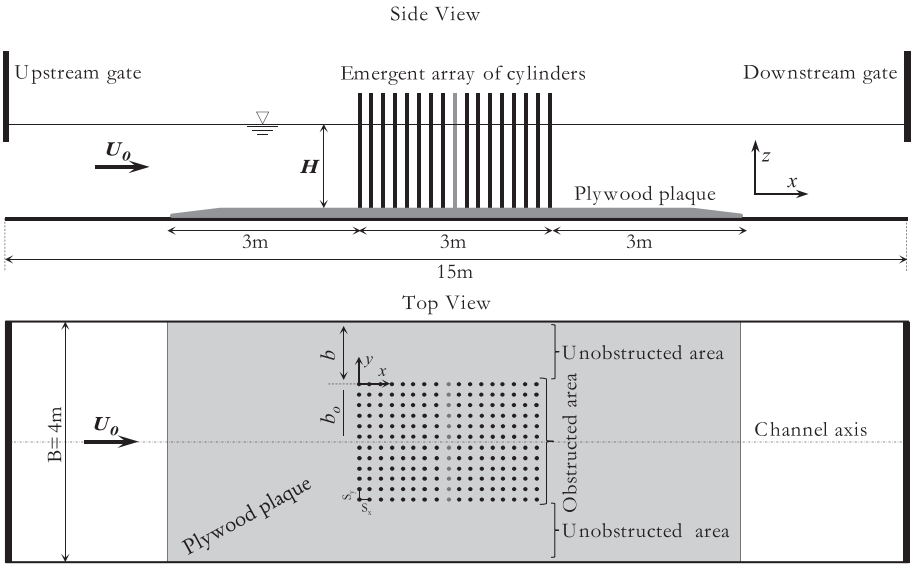


Fig. 3. General sketch of the laboratory flume with the experimental area. z is the vertical coordinate.

and correlation coefficient <70%) were also removed. Additional details concerning the channel setup and the ADV operation can be found elsewhere in Ben Meftah et al. (2007, 2008) and Ben Meftah et al. (2010).

The initial experimental conditions and some parameters of the investigated runs are shown in Table 2, where T is the water temperature, C_D is the cylinder drag coefficient, obtained using a procedure presented in Ben Meftah and Mossa (2013), $Re_0 = U_0H/\nu$ is the inlet Reynolds number, $Re_2 = U_2H/\nu$ is the free-stream Reynolds number, ν is the fluid kinematic viscosity, β and Φ are empirical constants. It is worth mentioning that, in Table 2, the runs with the same C_r differ for the U_0-values. The solid fraction of cylinders for all the experimental runs is $\varphi = 0.0028$.

In addition to the experimental data of the present study, in Table 2 we also illustrate the data obtained by White and Nepf (2007, 2008) for five other different configurations, of various values of C_Da, with the aim to reflect the cylinder-array-density effect on the flow structure. In the current study, the White and Nepf's (2007, 2008) velocity data were digitalized from Fig. 16 of their paper (White and Nepf, 2008). It is worth mentioning that in White and Nepf (2007, 2008) the shear layer thickness (δ_0) was determined as $(U_2\text{-}U_m)/\partial U/\partial y|_{ym}$, which differs from the definition of δ_2 used in this study. In the present study, the White and Nepf's (2007, 2008) δ_2 (Table 2) was determined, using the digitalized velocity data, as the transversal distance between y_m and the position where U is equal to $0.99U_2$.

Table 2
Initial experimental conditions and some parameters of the investigated runs: NI stands for not identified.

Runs	T (°C)	C_Da (cm^{-1})	C_r (–)	H (cm)	U_0 (cm/s)	y_m (cm)	U_m (cm/s)	δ_2 (cm)	U_2 (cm/s)	Re_0 (–)	Re_2 (–)	u^* (cm/s)	K_s (cm/s)	α (–)	β (–)	Φ (–)
	Present study															
R0	12.5	0.015	3.21	28	8.93	1.87	8.567	28.02	18.17	20,313	41,341	1.30	7.56	1.87	0.22	1.08
R1	20.0	0.015	3.21	25	10.00	2.9	7.12	22.59	21.79	25,000	54,482	1.18	5.13	2.71	0.24	1.01
R2	9.0	0.017	3.21	22	11.36	2.4	9.04	25.50	24.81	18,125	39,567	1.34	4.87	2.65	0.23	1.08
R3	14.0	0.014	3.21	18	13.89	2.47	11.08	25.49	30.94	21,250	47,334	1.34	3.91	3.41	0.23	1.10
R4	15.0	0.012	3.21	14	17.86	1.89	14.74	24.81	38.53	21,875	47,193	1.46	2.98	3.47	0.21	1.03
R5	13.0	0.014	3.21	12	20.83	2.48	15.60	24.43	43.05	20,625	42,622	1.60	3.47	3.99	0.23	1.06
R6	12.5	0.016	1.05	28	8.93	3.14	4.79	44.65	15.29	20,313	34,773	1.00	10.21	1.98	0.19	1.05
R7	12.3	0.016	1.05	25	10.00	4.11	5.73	39.49	16.79	20,188	33,890	0.95	8.69	2.59	0.22	1.05
R8	12.4	0.015	1.05	22	11.36	4.5	6.71	35.35	18.94	20,250	33,747	0.95	7.42	3.01	0.23	1.02
R9	12.6	0.015	1.05	18	13.89	4.6	8.39	36.70	23.46	20,375	34,414	0.89	5.79	4.02	0.24	1.05
R10	13.0	0.014	1.05	14	17.86	3.79	11.01	34.95	30.98	20,625	35,784	0.89	4.25	4.87	0.22	0.98
R11	13.3	0.015	0.36	14	17.86	7.01	9.94	32.10	26.65	20,813	31,055	1.55	10.10	2.99	0.28	0.99
R12	14.4	0.014	0.36	12	20.83	6.83	11.73	32.91	31.95	21,500	32,970	1.61	8.64	3.24	0.26	0.96
R13	13.8	0.015	0.36	18	13.89	6.02	7.13	43.63	19.79	21,125	30,097	1.18	10.34	2.67	0.25	1.13
R14	14.2	0.016	0.36	22	11.36	5.82	5.66	35.98	15.52	21,375	29,197	1.05	12.15	2.34	0.25	1.01
R15	14.5	0.016	0.36	25	10.00	4.85	4.55	44.09	13.47	21,563	29,050	1.10	17.77	1.80	0.22	1.03
R16	12.6	0.015	0.16	25	10.00	2.35	3.79	36.76	11.85	20,375	24,152	1.38	33.66	1.10	0.19	1.02
R17	13.3	0.014	0.16	18	13.89	3.14	6.06	34.49	18.32	20,813	27,449	1.84	21.31	1.34	0.20	1.03
R18	14.0	0.014	0.16	12	20.83	3.99	10.09	26.94	29.22	21,250	29,803	2.24	10.67	1.93	0.23	0.99
R19	14.5	0.016	0.16	28	8.93	2.45	3.84	40.98	11.06	21,563	26,706	1.30	38.05	1.08	0.20	1.04
	White and Nepf (2007, 2008)															
I	NI	0.092	0.50	6.8	NI	1.19	7.15	27.50	17.67	NI	20,000	1.92	20.83	1.06	0.19	1.01
IV	NI	0.285	0.50	6.6	NI	1.81	7.27	26.66	17.34	NI	1800	2.34	41.03	0.97	0.22	1.01
VI	NI	0.255	0.50	6.0	NI	1.05	4.92	35.20	12.32	NI	10,000	1.48	36.35	0.88	0.18	1.02
VII	NI	2.430	0.50	6.6	NI	1.61	5.93	30.16	16.83	NI	2900	2.25	41.23	0.92	0.19	1.06
X	NI	1.770	0.50	7.8	NI	1.01	10.98	30.57	29.87	NI	28,000	3.95	50.03	0.79	0.16	0.99

It is also worth mentioning that the transversal profiles of the flow velocity were made at mid-depth ($z = 0.5H$). According to White and Nepf (2007, 2008), the mid-depth measurements were within 5% of the depth-averaged velocity, confirmed by several vertical velocity profiles, which showed the velocity to be nearly uniform over depth within the vegetation, and to have a standard logarithmic profile in the open channel. The same observation was also confirmed in Ben Meftah and Mossa (2013). Therefore, in this manuscript, for the sake of simplicity, we address to the flow properties at mid-depth in terms of representative the mean flow characteristics.

4. Results and discussion

4.1. Shear layer development

Fig. 4 shows an example of a typical map of the distribution of the measured longitudinal velocity component U in both the obstructed and the unobstructed flow domains. The transversal profiles of U refer to run R3. The solid curve qualitatively represents the position of the nominal limit of the shear layer as a function of the ratio x/x_{eq}, where x_{eq} is the downstream position at which the fully-developed flow state is achieved. By the dashed line we indicate the interface between the obstructed and the unobstructed areas. Fig. 4 clearly shows the effects of the array of cylinders on the flow structures. In this context it is important to mention that the flow patterns within the obstructed area have been largely discussed in a previous study of Ben Meftah et al. (2014). Moreover, the flow interaction within an emergent array of cylinders/vegetation has been also commonly analyzed in Ben Meftah and Mossa (2013). In the unobstructed area, at $y/b > 0$, the U-profiles, for $x/x_{eq} \geqslant 0.1$, show the development of two typical regions: (i) a region immediately next to the obstructed-unobstructed interface, where U increases gradually from a certain velocity ($U > 0$) at the interface ($y = 0$) to a full velocity U_2, defined as the shear layer, and (ii) a free-stream region where U remains almost constant and equal to the full velocity U_2.

Fig. 4 clearly shows the development of the shear layer along the interface, having a feature of a gradually-increasing width in the downstream direction. Near the leading edge of the array, at $x/x_{eq} \leqslant 0.11$, the width of the shear layer grows smoothly, resembling in form the prototypical growth of the boundary layer in the initial laminar region over a flat-plate (Schlichting, 1955). From $x/x_{eq} > 0.11$ to $x/x_{eq} \approx 0.51$, the shear layer width undergoes a sharp increase. Further downstream, at $x/x_{eq} > 0.91$, the width of the turbulent shear layer tends to an almost constant value, where a fully-developed flow state is achieved. White and Nepf (2007) observed that as the shear layer width increases, the shear in the outer layer decreases indicating a net flux of momentum toward the shear layer. This momentum penetration is limited by the drag of the array of cylinders. At the downstream position x_{eq}, a maximum momentum penetration should be established leading to an equilibrium state of constant shear layer width (White and Nepf, 2007, 2008; Ben Meftah et al., 2014). Huai et al. (2015), making large-eddy simulation (LES) of turbulent rectangular open-channel flow with an emergent rigid vegetation patch, which is very similar to the model geometry investigated in this manuscript, proposed a phenomenological model, based on numerical results, for the evolution process in the vegetation flow. The model divided the entire flow region into four zones: an initial flow zone, a diverging flow zone, a developing zone and a fully-developed zone. In Fig. 4 three of the four zones are clearly shown: the diverging flow zone ($x/x_{eq} < 0.11$), the developing zone ($0.11 \leqslant x/x_{eq} \leqslant 1$) and the fully-developed zone ($x/x_{eq} \geqslant 1$). Huai et al. (2015) indicated that the velocity difference U_2-U_1 (see Fig. 2) creates a shear layer (mixing layer) near the vegetation edge, and Kelvin-Helmholtz vortices evolve downstream. In the fully-developed zone, the flow turbulent structures grow to a finite size and reach a fixed distance of penetration into the canopy and the velocity within and outside the vegetation patch is basically uniform ($\partial U/\partial x \approx 0$). The numerical results of Huai et al. (2015) are qualitatively in good agreement with the experimental results of the current study. The Instantaneous velocity distribution in Huai et al. (2015) clearly shows the flow vortical structure in the obstructed-unobstructed area, which is not the case in Fig. 4, this is because the LES is much more powerful for the examination of the trajectory of turbulent motions than the point measurements by the ADV.

4.2. Effect of C_r on the flow hydrodynamic structure

Fig. 5 shows an example of the mean flow velocity distribution in the unobstructed domain ($y/b \geqslant 0$). The experimental data refer to runs R1, R7, R15 and R16. The transversal profiles correspond to the downstream position at $x/x_{eq} = 1.01$, where the fully-developed zone is achieved. Runs R1, R7, R15 and R16 were carried out under the same initial hydraulic condition, same values of U_0 and H (see Table 2), but of different values of C_r, ranging between 0.16 and 3.21. The transversal profiles of U/U_0 show the same general trend as a function of y/b, indicating, however, a sharp shifting from each other as y/b further increases. Fig. 5 shows that U/U_0 gradually increases from the edge of the obstructed area ($y/b = 0$) toward the free-stream region where it attains an almost constant value of order U_2/U_0. The shear layer is located between the interface ($y/b = 0$) and the transversal position y/b at which $U/U_0 \approx U_2/U_0$. Nearby the interface ($y/b < 0.2$), U/U_0 almost increases linearly, with a slight and unpredictable dependence on C_r, and then goes up in a logarithmic fashion, showing a significant dependence on

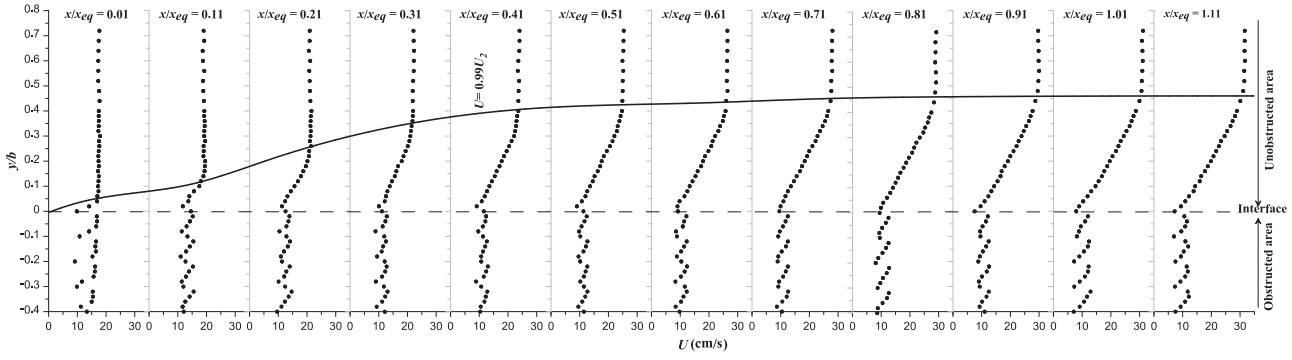


Fig. 4. Map of the U-velocity distribution for Run R3. The solid curve qualitatively represents the nominal limit of the shear layer, obtained at $U(y) = 0.99U_2$.

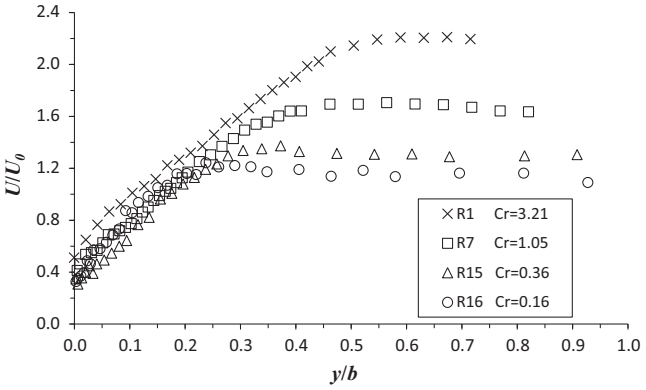


Fig. 5. C_r-effect on the mean flow velocity.

C_r, until reaching its maximum value (U_2/U_0) at a certain position y/b, also appeared variable as a function of C_r. Fig. 5 indicates an obvious rise of the free-stream velocity U_2/U_0 as C_r increases. Since all runs have the same value of U_0, this implies that the free-stream velocity U_2 significantly increases as C_r increases, which is more pronounced with $C_r = 1.05$ and 3.21. For small values of C_r, i.e., 0.16 and 0.36, U_2 is slightly increased with the increase of C_r. Based on the present results, it can be concluded that, in real channel flow partially obstructed by emergent vegetation, an increase of C_r could increase the risk of erosion of the channel bed and banks.

Fig. 6 depicts the transverse profiles of the time and space-averaged of both the streamwise U and the spanwise V velocities in addition to their resultant $[(U^2 + V^2)^{0.5}]$, represented in vector form. U and V at the obstructed domain are determined as $(1/s_y)\int U dy$ and $(1/s_y)\int V dy$ over the transversal spacing between cylinders s_y. Data refer to Runs R5 (Fig. 6a) and R11 (Fig. 6b) of C_r equal to 3.21 and 0.36, respectively. The flow velocity profiles were taken from the channel axis, at the center of the obstructed area, until nearly the left wall-side of the channel, in the unobstructed area. All profiles refer to the developing zone at the downstream position $x/x_{eq} = 0.61$. It is worth mentioning that the profiles correspond to a position midway between two consecutive lateral rows of cylinders, distanced 8.34d from each other.

In the obstructed domain, Fig. 6 shows that, nearby the channel axis for both runs, the velocity vectors are strongly influenced by their y-positions relative to a cylinder position (Ben Meftah et al., 2015). At a close position to a cylinder, their magnitudes significantly decrease and then increase monotonically to reach their maximum values (peaks) at midway between two side-by-side cylinders. In the center of the obstructed area (nearby the channel axis), it can be also noted that the velocity vectors are almost in-line with the mean flow direction, showing transversal profiles of parabolic shape. These profiles are expected to be a periodic function in y whose period is s_y (Ben Meftah and Mossa, 2013), which is more pronounced with run R5. As going further toward the interface between the obstructed and the unobstructed domains, the velocity vectors undergo considerable modifications: (i) they experience gradual deviations (toward the interface) relative to the mean flow direction, (ii) the peaks of the velocity vectors are not midway between two side-by-side cylinders, but they take place more and more close to the left cylinder, and (iii) their parabolic profiles, observed nearby the channel axis, disappear showing instead a "*saw-teeth*" shape near the interface (Ben Meftah et al., 2014). Similar flow behavior was numerically obtained by Huai et al. (2015). Moreover, Fig. 6 shows that U slightly decreases as going toward the interface (as y increases), reaching a minimum value at the interface ($y = 0$). In contrast, V undergoes a gradual increase as a function of y. The spanwise velocity V, on the contrary of U, reaches its maximum at a certain distance away from the interface ($y = 0$) in the shear layer and then stars to gradually decrease, reaching very small values in the free-stream region. The deviation of the flow resultant velocity toward the interface,

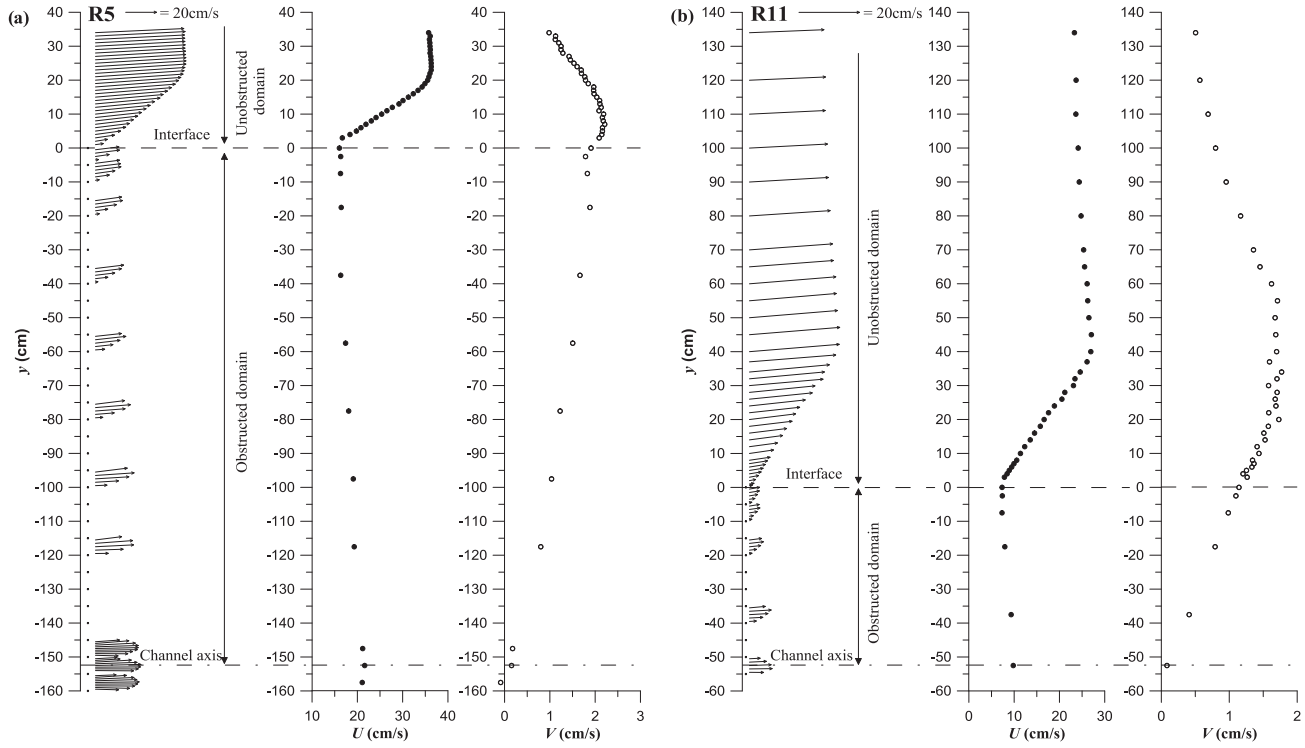


Fig. 6. C_r-effect on the flow velocity structure for runs R5 and R11, the equidistant points (vector representation) in the obstructed domain indicate the lateral row of cylinders downstream which the measurements of the velocity profiles were done.

the decrease of U and the increase of V confirm the lateral flow diversion (mass transfer) from the decelerating flow in the obstructed area to the accelerating flow in the parallel unobstructed area, caused by the drag of the cylinders/vegetation arrays, as also mentioned in previous studies (e.g., Naot et al., 1996; Vermaas et al., 2011; Ben Meftah et al., 2014; Yang et al., 2015).

On the other hand, Fig. 6 also shows the flow structures as varying the contraction ratio C_r. The most important observation from Fig. 6 is the significant increase of the mean flow velocity as C_r increases. Despite the comparable values of the channel mean velocity U_0 upstream of the obstructed area, which is 21 cm/s for run R5 against 18 cm/s for run R11, the free-stream velocity U_2 is of order 43 cm/s with R5 against 27 cm/s with R11 (Table 2). As it be seen, U_2 is almost doubled as C_r passes from a value of 0.36 to 3.21, which is also clearly shown in Fig. 5. For $C_r = 3.21$, Fig. 6 shows that the development of the shear layer may be confined by the channel wall-side. However, with $C_r = 0.36$, the shear layer appears developed without (or with a minimum) effect of the wall-side. The reduction of the channel wall-side effect, as C_r decreases, is manifested by a slight variation of the free-stream velocity profile, as shown in Run R11, where U undergoes a gradual decline after reaching its maximum value U_2.

Fig. 7 depicts the profiles of the free-stream velocity U_2 normalized by U_0 and plotted versus the contraction ratio C_r in semi-logarithmic form, for all runs (R0 to R19). Fig. 7 shows that with the same value of C_r the flow velocity U_2/U_0 tends to collapse into a single point of an almost constant value, independent of the flow characteristics, i.e., the Reynolds numbers as shown in Table 2. As C_r increases, however, U_2/U_0 increases, following almost a single curve of logarithmic fashion, as shown by the regression line, as:

$$\frac{U_2}{U_0} = 0.289Ln(C_r) + 1.758 \quad (R^2 = 0.94) \tag{2}$$

where R^2 is the correlation coefficient.

Fig. 8 shows the variations of the maximum level of the flow turbulence as a function of C_r in the unobstructed domain ($y \geqslant 0$). It is worth mentioning that, as observed in previous studies (e.g., White and Nepf, 2007, 2008; Ben Meftah et al., 2014; Huai et al., 2015), the maximum of the flow turbulence levels mostly occur within the shear layer flow-field, near the interface ($y = 0$). Fig. 8(a) shows the variation of the streamwise turbulence intensity $(U')_{max}/U_2$, where $(U')_{max}$ indicates the maximum value of the u'-root mean square $U' = [(1/(N-1))\Sigma(u'^2)]^{0.5}$, u' is the streamwise velocity fluctuation and N (18,000) is the number of velocity samplings. Fig. 8(b) illustrates, however, the variation of the maximum value of the spanwise Reynolds stress $-(U'V')_{max}$ normalized by the square free-stream velocity $(U_2)^2$, where $U'V' = (1/(N-1))\Sigma(u'v')$ is the time-averaged shear stress and v' is the spanwise velocity fluctuation. The instantaneous velocity is defined as $u_i(t) = U_i + u_i'(t)$, where $U_i = (U, V)$, $u_i' = (u', v')$ and t denotes the time. In Fig. 8(b) we also plot the data obtained by White and Nepf (2008) for other five different configurations (see Table 2), with the aim to reflect the array density effect on the flow structure.

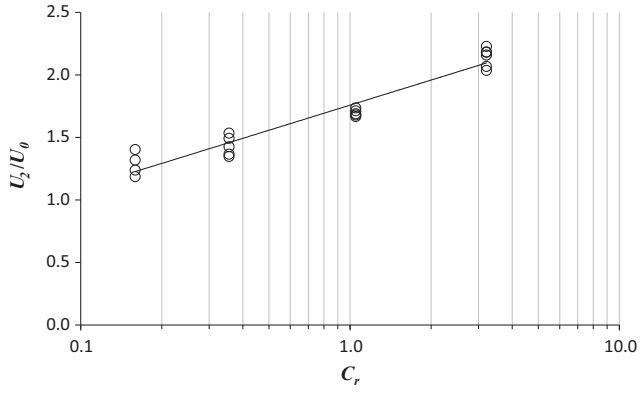


Fig. 7. C_r-effect on the free-stream flow velocity for all runs.

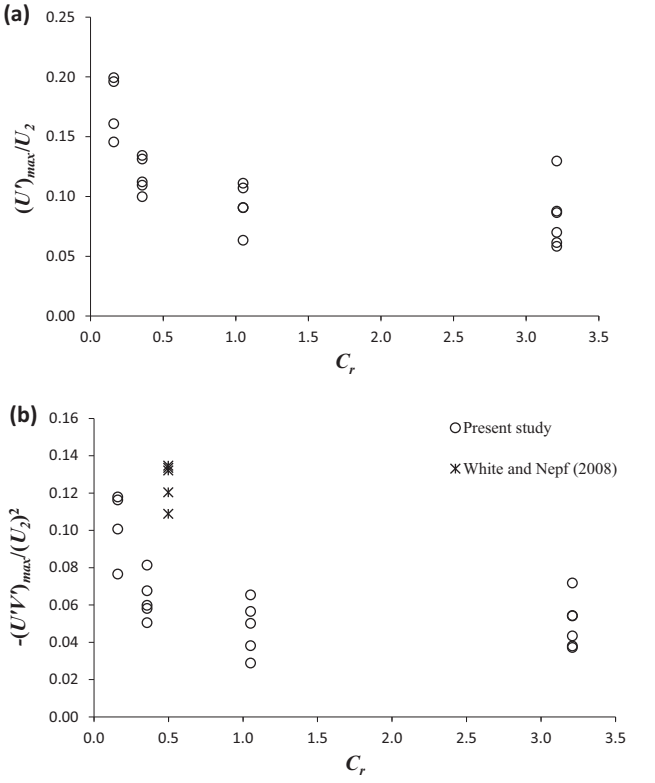


Fig. 8. C_r-effect on the flow turbulence, (a) on the maximum values of the streamwise turbulence intensity, (b) on the maximum values of the spanwise Reynolds stress.

Fig. 8 indicates that the flow turbulence show a general downward trend as C_r increases. For values of $C_r \leqslant 1.01$, the streamwise turbulence intensity and the Reynolds stress strongly decline as C_r goes up, while for $1.01 \leqslant C_r \leqslant 3.21$, both of them almost stay at the same level. The data of White and Nepf (2008), illustrated in Fig. 8 (b), show that, for $C_r = 0.5$, the Reynolds stress is increased from a predictable averaged value O(0.05), obtained based on the data tendency of the present study, to a value O(0.12). This substantial increase in the shear stress can be explained by the high array density in White and Nepf (2008) as compared to that of the present study (see C_Da values in Table 2).

In order to get a general trend of the maximum flow turbulence intensity as a function of the contraction ratio C_r, in Fig. 9 we plot the averaged-values of $(U')_{max}/U_2$ and $-(U'V')_{max}/(U_2)^2$, obtained as the average of the measured values for each C_r, as shown in Fig. 8. The vertical bars indicate the value of the standard deviation (variability) of both parameters. Fig. 9 clearly indicates the general downward trend, as previously mentioned, of these parameters as a function of C_r. The data plotted in Fig. 9 yield the following empirical equations to predict approximate values of the flow turbulence as a function of C_r:

$$\frac{(U)'_{max}}{U_2} = 0.1012C_r^{-0.244} \quad (R^2 = 0.91) \tag{3}$$

$$\frac{-(U'V')_{max}}{(U_2)^2} = 0.057C_r^{-0.236} \quad (R^2 = 0.76) \tag{4}$$

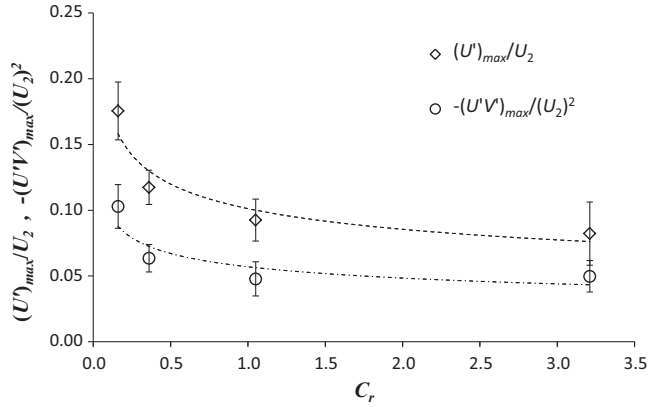


Fig. 9. General trend of the maximum values of the flow turbulence intensity and the Reynolds shear stress as a function of C_r.

It is worth mentioning that the applicability of these equations is limited to hydraulic conditions similar to those presented in this manuscript, i.e., a square arrangement of the array of cylinders/vegetation with low density, a Reynolds number $O(2 \times 10^4–5 \times 10^4)$, a contraction ratio C_r O(0.1–0.4).

4.3. Determination of k_s adapting the Prandtl's log law modified by Nikuradse

In the fully-developed zone ($x/x_{eq} \geqslant 1$), Fig. 4 clearly shows the development of the shear layer along the interface between the obstructed and the unobstructed domains. Within the shear layer, the transversal profiles of the streamwise velocity at mid-depth, also denoted as the mean flow velocity, behaves in a similar way as a vertical velocity profile above aquatic submerged vegetation (Järvelä, 2005; Stephan and Gutknecht, 2002), as shown in Table 2. From the array edge ($y/b > 0$), U starts to gradually increase in a linear trend until it reaches a certain transversal position, from which it continuous to going up following a logarithmic fashion, and then reaches the constant free-stream velocity U_2. Since the shear layer is developed under the drag generated by the array of cylinders/vegetation through the water column, a good description of the transversal velocity profile within the shear layer could lead to define the flow resistance. In analogy with previous results obtained in submerged vegetated channels (e.g., Järvelä, 2005; Stephan and Gutknecht, 2002) we will try to determine the characteristic hydrodynamic roughness height k_s (equivalent sand roughness), following the universal logarithmic law presented in Eq. (1).

In this study, analogous to the procedure used with submerged vegetated channels, in Eq. (1) the integration constant C and the von Karman constant κ are kept equal to 8.5 and 0.4, respectively. To enable the computation of the roughness height k_s, the shear velocity u^* must be estimated. In the present study the shear velocity is determined as $u^* = [-(U'V')_{max}]^{1/2}$, for the profiles measured at the downstream position $x/x_{eq} = 1.01$ in the fully-developed zone. As defined above, y_m is determined as the zero plane displacement of the logarithmic profile, obtained experimentally based on the linearity of the measured streamwise velocity profiles in semi-logarithmic coordinates. Fig. 10(a) shows an example (run R6) of how we determined y_m, as the value that provided the best fit between the experimental data and a general logarithmic profile. Fig. 10(a) indicates that the flow velocity starts to follow the logarithmic trend at a certain transversal position y > 0, away from the interface, until the nominal limit of the shear layer, obtained at $U(y) = 0.99U_2$.

After determining y_m (Table 2) using the procedure shown in Fig. 10(a), in Fig. 10(b) we plot the dimensionless flow velocity,

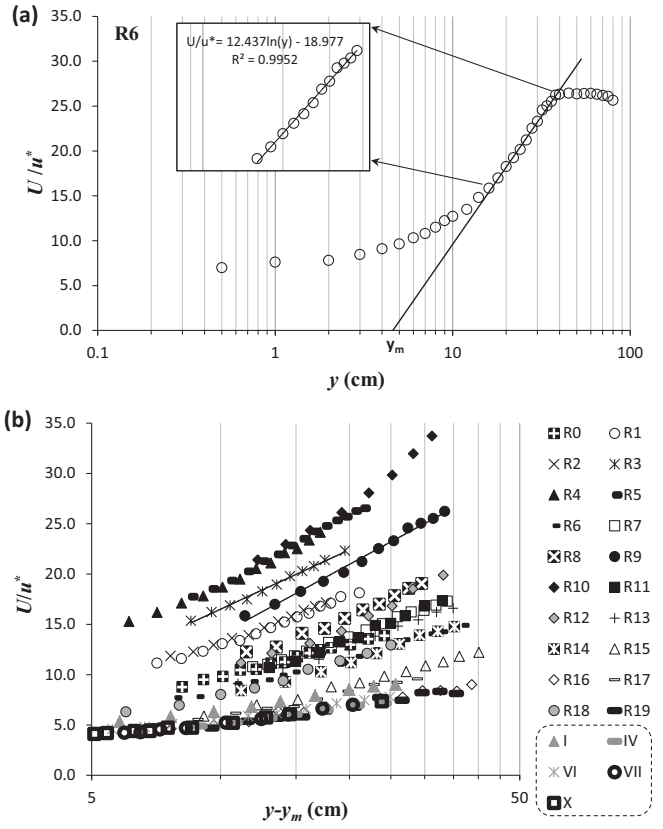


Fig. 10. Logarithmic trend of the flow velocity, (a) procedure to determine the zero plane displacement of the logarithmic profile y_m and (b) U/u^* against $(y - y_m)$ in semi-logarithmic form. Runs I, IV, VI, VII and X are the data obtained by White and Nepf (2008) at the fully-developed zone.

of logarithmic trend for all runs, U/u^* versus $(y - y_m)$, in semi-logarithmic scale graph. In addition to the experimental data of the present study, in Fig. 10(b) we also plot the data obtained by White and Nepf (2008) with the five different values of the array density (see Table 2). As clearly shown in Fig. 10(b), for each run, U/u^* fits a perfect regression line as a function of $(y - y_m)$, as shown, for example, by the solid line with runs R3 and R9. It is clearly noted from Fig. 10(b) that the data regression lines show different slopes, varying from a run to another. This implies that the slope associated with the measured velocity profiles, represented in Eq. (1) as $(1/\kappa)$, does not always coincide with the standard values 2.5, obtained with a von Karman coefficient $\kappa = 0.4$, as reported for flows over smooth and rough walls. Similar results were observed by Manes et al. (2011), studying the effects of wall permeability on the turbulent boundary layer. It is interesting to note that in other procedures, as reported in Stephan and Gutknecht (2002), the zero plane displacement y_m was evaluated as the value that forced the profile of $(y - y_m)(\partial U/\partial y)$ to be constant $(=1/\kappa)$. In the present study, we observed that this "enforced procedure" strongly affect the linearity of the U-velocity profile in the semi-logarithmic coordinates, as shown in Fig. 10(a).

Based on the flow velocity profiles illustrated in Fig. 10(b), obtained after the determination of y_m following the procedure previously explained, the different slopes of the data regression lines allows us to modify Eq. (1) as:

$$\frac{U}{u^*} = \frac{\alpha}{\kappa} Ln\left(\frac{y - y_m}{k_s}\right) + C = \frac{1}{\kappa} Ln\left(\frac{y - y_m}{k_s}\right)^{\alpha} + C \quad (5)$$

where α is a coefficient to be determined, for each run, using the slopes of the regression lines plotted in Fig. 10(b). The different

values of α are illustrated in Table 2. Fig. 11 depicts the mean velocity profiles, of the dimensionless velocity U^+ as a function of the dimensionless coordinate $(y^+)^\alpha$, in semi-logarithmic coordinates, where $U^+ = U/u^*$ and $y^+ = (y - y_m)/k_s$. The data obtained by White and Nepf (2008) are also plotted in Fig. 11. Using this scaling technique, Fig. 11 shows a perfect collapse of the different profiles into a single straight profile of a $1/\kappa$ slope.

The superior limit of Eq. (5), applied at $(y - y_m) = \delta_2$ where $U = U_2$, indicates that α could be a logarithmic function in U_2/u^*. The coefficient α obtained from the fitting velocity profiles, shown in Fig. 10(b) for the present study and those of White and Nepf (2008), is plotted versus the normalized velocity U_2/u^* in Fig. 12. Fig. 12 clearly shows that, independent of the array characteristics (configuration type and density), all the data of both studies collapse into a single profile, leading to the following relationship:

$$\alpha = 2.452Ln\left(\frac{U_2}{u^*}\right) - 4.261 \quad (R^2 = 0.96) \tag{6}$$

An easy applicability of Eq. (5) to predict the mean flow velocity also requires the determination of the flow hydrodynamic properties y_m and k_s. It is worth mentioning that α can be determined using Eqs. (6) and (2), for the prediction of U_2.

According to the procedure used in the present study to determine the zero plane displacement y_m, the logarithmic function of the regression lines [Fig. 10(a)], applied at $y = y_m$, indicates that y_m could be a power function in $\exp(1/\alpha)$. In Fig. 13(a) we plot the dimensionless zero plane displacement y_m/b versus $\exp(1/\alpha)$. In addition to the data of the present study, the data of White and Nepf (2008) are also plotted. For both studies, independent of the array density, Fig. 13(a) indicates that the data almost collapse into a single curve of good downward trend of y_m/b as a function of $\exp(1/\alpha)$, leading to the following equation:

$$\frac{y_m}{b} = 0.07[\exp(1/\alpha)]^{-1.435} \quad (R^2 = 0.84) \tag{7}$$

Similar to y_m the hydrodynamic roughness height k_s could be also a power function in $\exp(1/\alpha)$. Fig. 13(b) illustrates the variation of k_s, normalized by the width of the unobstructed area b, as a function of $\exp(1/\alpha)$. Fig. 13(b) shows that the data almost collapse into a single curve. Despite the large difference between the vegetation densities simulated in the present study and those in White and Nepf (2008), as shown in Table 2, the data of both studies almost fit the same profile in a continuous way. This confirm a general trend, independent of the array density, of k_s/b as a function of α, giving the following expression to predict k_s:

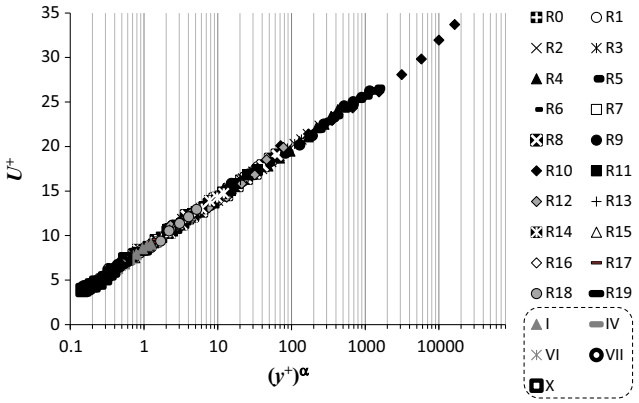


Fig. 11. Mean velocity profiles of logarithmic trend plotted as U^+ versus $(y^+)^\alpha$. Runs I, IV, VI, VII and X are the data obtained by White and Nepf (2008) at the fully-developed zone.

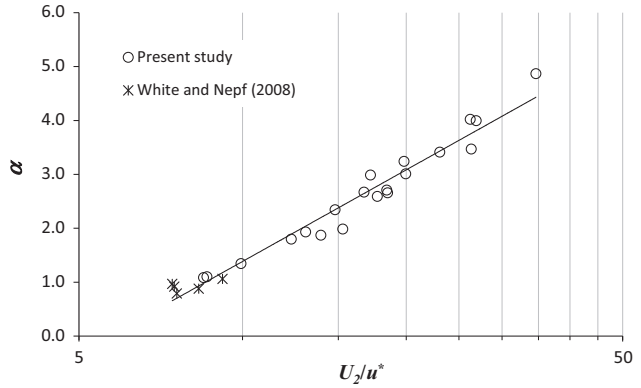


Fig. 12. Variation of the coefficient α as a function of the normalized free-stream velocity U_2/u^*.

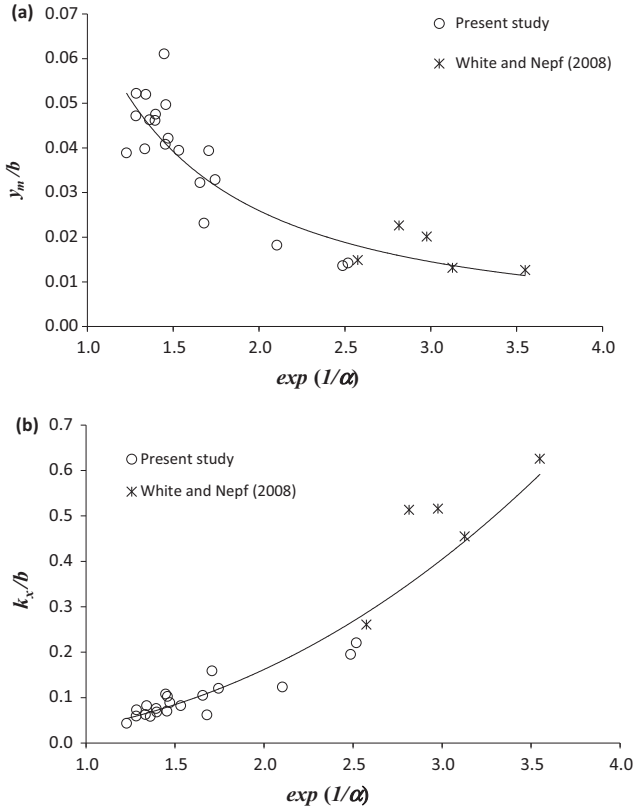


Fig. 13. Trend as a function of α for; (a) the zero plane displacement y_m, (b) the hydrodynamic roughness height k_s.

$$\frac{k_s}{b} = 0.034[\exp(1/\alpha)]^{2.257} \quad (R^2 = 0.91) \tag{8}$$

Until now, the experimental results treated in this study, including those recently obtained by White and Nepf (2008), clearly demonstrate that the transversal profile of the mean flow velocity, at the interface between the obstructed and the unobstructed domains, undergoes a logarithmic trend. This, and by analogy with previous studies on submerged vegetated channels, is allowed us to represent it as a roughness-induced velocity profile, which giving experimental determination of the hydrodynamic roughness height k_s. Results also show that k_s in addition to other flow hydrodynamic properties implicitly/explicitly depend on the contraction ratio C_r. The velocity profiles of logarithmic trend are represented by the universal log-law shown in Eq. (5),

with specific slight modification. With the purpose to easily apply the proposed log-law, a series of empirical equations, i.e., Eqs. (2) and (6–8), is suggested to predict the flow hydrodynamic characteristics forming Eq. (5).

4.4. Similarity of the velocity profiles

Despite the perfect collapse of the velocity profiles into a single logarithmic curve, as shown in Fig. 11, it was observed that the modified log-law proposed in Eq. (5) suffers from a defect. It is not appropriate to represent all the data onto a single profile. It can be noted that the starting and ending coordinates (y^+) of the profiles vary from a run to another, as shown in Fig. 14. The incomplete similarity between the velocity profiles, following the scaling mode proposed in Eq. (5), makes us to think for other compatible scalings to better represent the entire mean velocity profiles in the obstructed area, respecting always the log-law approach. According to previous studies of Ben Meftah et al. (2014) and Ben Meftah and Mossa (2016), the rescale of the velocity and the length variables, using the flow velocity U_2, U_m and the width of the shear layer δ_2 instead of k_s, in the following way:

$$U^{++} = \frac{U - U_m}{U_2 - U_m} \text{ and } y^{++} = \frac{y - y_m}{\delta_2} \tag{9}$$

shows a complete similarity between the different velocity profiles of U^{++} as a function of y^{++}. The authors confirmed that the use of this scaling mode always represents the velocity profiles in complete similarity independent of the flow and cylinders/vegetation characteristics, i.e. the Reynolds number, the Froude number and the array density.

Taking into account this new rescaling mode, as presented in Eq. (9), Eq. (5) can be rewritten as follows:

$$\frac{(U - U_m)}{(U_2 - U_m)} = \frac{\alpha u^*}{(U_2 - U_m)} \frac{1}{\kappa} Ln\left(\frac{y - y_m}{\delta_2}\right) + \frac{\alpha u^*}{(U_2 - U_m)} \frac{1}{\kappa} Ln\left(\frac{\delta_2}{k_s}\right) + \frac{Cu^* - U_m}{(U_2 - U_m)} \tag{10}$$

It is can be noted that Eq. (10) is similar in form as Eq. (5), yielding to a new general equation of U^{++} as a function of y^{++} as:

$$\begin{cases} U^{++} = \frac{\beta}{\kappa} \ln(y^{++}) + \Phi \\ \text{where} \\ \beta = \frac{\alpha u^*}{(U_2 - U_m)} \\ \Phi = \frac{\alpha u^*}{(U_2 - U_m)} \frac{1}{\kappa} \ln\left(\frac{\delta_2}{k_s}\right) + \frac{Cu^* - U_m}{(U_2 - U_m)} = \frac{\beta}{\kappa} \ln\left(\frac{\delta_2}{k_s}\right) + \frac{Cu^* - U_m}{(U_2 - U_m)} \end{cases} \tag{11}$$

Using the measured values (Table 2) of the flow variables shown in Eq. (11), the coefficients β and Φ were easily determined, as illustrated in Table 2. Since at $y^{++} = 1$, $U^{++} = 1$, applying of Eq. (11) at this position gives the exact value of Φ, which is equal to 1. This implies that Φ is a constant, independent of the flow and the vegetation characteristics. The values of Φ, illustrated in Table 2 and determined using the measured data, are almost of order 1, with a standard deviation of 4%, confirming that Φ is a constant. An examination of the values of β, as illustrated in Table 2, shows that the latter is also a constant of order 0.22, with a standard deviation of 3%.

Fig. 15 shows the transversal profiles of the experimental rescaled velocity U^{++} as a function of y^{++}, plotted in a semi-logarithmic form. In addition to the data of the present study, the data of White and Nepf (2008) are also plotted in Fig. 15. Fig. 15 clearly shows that all the data, of the different runs, almost collapse into a single profile. In contrast to what happened in Fig. 14, where only a partial similarity occurs between the velocity profiles of logarithmic trend, Fig. 15 shows a complete similarity between the entire velocity profiles in the unobstructed area. On the same figure we also plotted the theoretical curve (gray solid line) of the normalized flow velocity U^{++}, represented by Eq. (11) with β and Φ equal to 0.22 and 1, respectively. Fig. 15 show that the experimental data follow the logarithmic fashion over $0.26 < y^{++} < 1$. In addition, we plot on the same figure the theoretical line of $U^{++} = y^{++}$ (dark dashed line). Fig. 15 indicates that the experimental data may be represented by the linear function $U^{++} = y^{++}$ over $y^{++} \leqslant 0.26$. For $y^{++} \geqslant 1$, the experimental data show that U^{++} is almost of order 1. It is worth mentioning that in this study, for $y^{++} \geqslant 1$, we observed that the magnitude of U^{++} is slightly affected by the contraction ratio C_r. U^{++} undergoes a slight and gradual reduction within the free-stream region ($y^{++} \geqslant 1$) with small values of C_r (see Fig. 6).

The plot of the mean flow velocity following the rescaling mode, reported in Eq. (9), is led to represent the entire transversal velocity profiles of all runs, in the unobstructed domain ($y^{++} \geqslant 0$), by a single typical profile. This typical profile shows an almost complete independence of the flow Reynolds number and the array density. Finally and according to the experimental results shown in Fig. 15, it can be concluded that the transversal mean flow velocity at the interface between the obstructed and unobstructed areas, in an open channel partially obstructed by an array of rigid and emergent cylinders/vegetation, can be easily predicted by a typical modified log-law as follows:

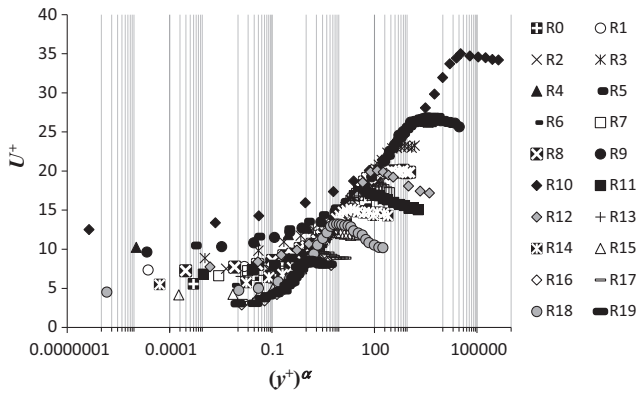


Fig. 14. Complete profiles of the mean velocity U^+ versus $(y^+)^\alpha$.

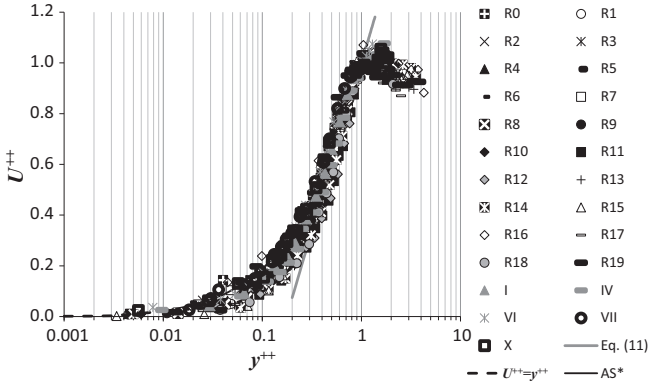


Fig. 15. Transversal profiles of U^{++} as a function of y^{++} in semi-logarithmic form. Runs I, IV, VI, VII and X are the data obtained by White and Nepf (2008) at the fully-developed zone. *By AS we indicate the analytical power-law solution proposed by Ben Meftah et al. (2014).

$$\begin{cases} U^{++} = y^{++} & \text{for} \quad 0 \leqslant y^{++} \leqslant 0.26 \\ U^{++} = \frac{\beta}{\kappa}\ln(y^{++}) + \Phi & \text{for} \quad 0.26 \leqslant y^{++} < 1 \\ U^{++} \approx 1 & \text{for} \quad y^{++} \geqslant 1 \\ \textit{with} \\ \beta \approx 0.22 \ \kappa = 0.4 \text{ and } \Phi = 1 \end{cases} \tag{12}$$

In order to compare the presented modified log-law (Eq. (12)) with other solutions proposed in literature, in Fig. 15 we also plot the analytical power-law solution proposed by Ben Meftah et al. (2014), indicated by AS on the figure. The analytical solution of Ben Meftah et al. (2014) is illustrated in Table 1. Fig. 15 clearly shows that the present modified log-law (Eq. (12)) quietly follows the analytical solution proposed by Ben Meftah et al. (2014). The difference between both solutions is that the present modified log-law is much more practical and much more stable (in term of determining the hydrodynamic properties and constants composing the equations) than the analytical solution in predicting the transversal velocity profile.

Fig. 16 depicts the profiles of the normalized shear layer width δ_2/b varies as a function of the contraction ratio C_r in semi-logarithmic form. On the same figure we also plot the data of White and Nepf (2008). Fig. 16 shows that δ_2/b is strongly affected by C_r rather than the flow hydrodynamic properties and the array density. δ_2/b increases as C_r increases following almost a logarithmic fashion as:

$$\frac{\delta_2}{b} = 0.109Ln(C_r) + 0.402 \quad (R^2 = 0.87) \tag{13}$$

In Fig. 17 we plot, for all runs, the velocity ratio U_m/U_2 versus C_r. Noting that the free-stream velocity U_2 can be predicted by Eq. (2). Fig. 17 clearly shows that U_m/U_2 is almost of the same magnitude at a given value of C_r. In addition, U_m/U_2 show a very slight variation in C_r. It randomly varies between values of 0.33–0.42, including the previous data obtained by White and Nepf (2008), against 0.16–3.21 for C_r. This implies that U_m/U_2 appears invariant in C_r. It can be seen that the values of U_m/U_2 obtained by White and Nepf (2008) are comparable to the values of the current study, which means that this velocity ratio is also independent of the array density. Therefore, the velocity ratio U_m/U_2 can be regarded as a constant value of order 0.36 (average of all the measured values presented in Fig. 17) as:

$$\frac{U_m}{U_2} \approx 0.36 \tag{14}$$

In the present study, the new modified log-law proposed in Eq. (12) avoids the measurement of some sensitive turbulence parameters, i.e., the shear stresses to predicted the friction velocity u^*, as shown in Eqs. (1) and (5). This is an important benefit which improve the practical applicability of the later. Another benefit of this study is that the hydrodynamic properties forming Eq. (12), i.e., U_2, U_m, δ_2, can be predicted by Eqs. (2), (13), and (14) using the initial hydraulic conditions (H, Q, C_r). Noting that y_m is of few centimeters away from the interface. An expression of y_m is proposed in Eq. (7) as function of α, which is in turn a function of u^*. In order to find another expression of y_m without the friction velocity, in Fig. 18 we plot the variation of y_m/b against the Reynolds number Re_2. Fig. 18 shows that, for $Re_2 < 3.10^4$, y_m/b slightly varies with Re_2 around a value of order 0.02. However, for $Re_2 \geqslant 3.10^4$, y_m/b starts to increase significantly with the increase of Re_2, following this expression:

$$\frac{y_m}{b} = 0.047Ln(Re_2) - 0.452 \quad (R^2 = 0.59) \tag{15}$$

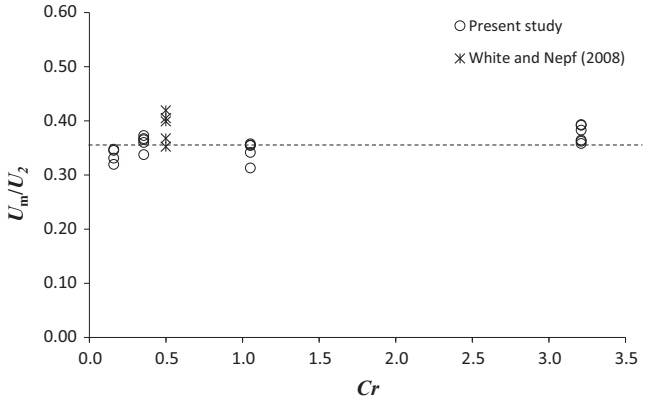


Fig. 17. Trend of U_m/U_2 as a function of the contraction ratio C_r.

5. Conclusions

Aquatic plants/macrophytes usually play a number of roles on the hydrodynamic behavior and environment dynamic equilibrium of rivers and estuaries. Natural vegetation in river floodplains and adjacent wetlands is characterized by various aspects (e.g., different types, different distributions, different densities) and can occupy the entire width or a portion of a waterway, reflecting a number of complex phenomena. Therefore, a good knowledge of the physical interaction between a flowing fluid and aquatic vegetation is required to promote best environmental management practice.

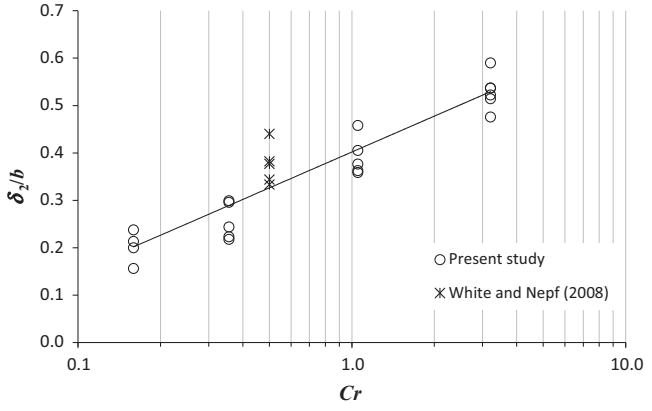


Fig. 16. Variation of the normalized shear layer width δ_2/b as a function of the contraction ratio C_r.

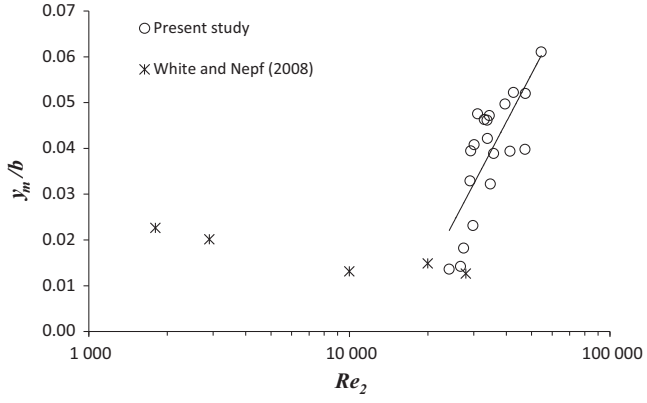


Fig. 18. Trend of y_m/b as a function of the Reynolds number Re_2.

In this manuscript, we focus on the study of the flow hydrodynamic structures in a channel partially obstructed by arrays of vertical, rigid, emergent, vegetation/cylinders. In the first part of Section 4, after analyzing the shear layer development, we give special attention to understand the effect of the contraction ratio C_r on the flow structures, that seems lacking in literature. In a second part, we analyze the transversal profiles of the mean flow velocity in the flow fully-developed zone. Since these profiles behave in a similar way as a vertical velocity profiles above aquatic submerged vegetation, showing logarithmic tendency, a characteristic hydrodynamic roughness height k_s is determined, adapting, by analogy, the Prandtl's log law modified by Nikuradse (1933). Finally, an improved modified log-law, predicting the representative transversal profile of the mean flow velocity, at the obstructed-unobstructed interface, is proposed.

The most significant results obtained in this study are summarized as follows:

(i) the measured flow velocity clearly shows the development of a shear layer immediately next to the obstructed-unobstructed interface. Adjacent to the shear layer, a free-stream region of full (constant) velocity flow is also formed. The entire flow region at the interface is divided into three zones: a diverging flow zone ($x/x_{eq} < 0.11$), a developing zone ($0.11 \leqslant x/x_{eq} \leqslant 1$) and a fully-developed zone ($x/x_{eq} \geqslant 1$);

(ii) a lateral flow diversion (mass transfer) from the decelerating flow in the obstructed area to the accelerating flow in the parallel unobstructed area, caused by the drag of the cylinders/vegetation arrays, is confirmed;

(iii) the contraction ratio C_r significantly affects the flow hydrodynamic structure. As C_r substantially increases the mean flow velocity, within the unobstructed area, undergoes considerable increase, which, in real cases of partially obstructed channel flows, could increase the risk of erosion of channel bed and banks. The experimental results also show that the width of the shear layer, the turbulence intensity and the Reynolds shear stress are significantly affected varying the contraction ratio;

(iv) Within the shear layer, of fully-developed flow, the transversal profiles of the mean flow velocity resemble the typical logarithmic profile of the vertical distribution of velocity in a rough channel. This allowed us to represent it as a roughness-induced velocity profile. Therefore and analogous to the procedure used with submerged vegetated channels, a characteristic hydrodynamic roughness height k_s is determined to define the vegetation resistance to the flow, adapting, by analogy, the Prandtl's log law modified by Nikuradse (1933). The experimental results show that k_s in addition to the other flow hydrodynamic properties implicitly/explicitly depend on the contraction ratio C_r. The slope associated with the measured logarithmic velocity profiles, represented in Eq. (1) as $(1/\kappa)$, does not always coincide with the standard values 2.5, obtained with a von Karman coefficient $\kappa = 0.4$, as reported for flows over smooth and rough walls. This made us to slightly modify Eq. (1), as shown in Eq.(5), in order to incorporate all the measured slopes into a single $1/\kappa$–slope;

(v) In this study, the use of a modified scaling mode (Eq. (9)) leads to a complete similarity between the different entire velocity profiles. The comparison of the current data with previous studies, carried out under other hydraulic conditions and vegetation configurations, indicates that all the transversal velocity profiles presented following the scaling mode proposed in Eq. (9) are characterized by a typical profile, independent of the contraction ratio, the flow Reynolds number and the array density. Finally, a general modified log-law, describing the typical transversal profile of the mean flow velocity, is proposed in this manuscript, as depicted in Eq. (12). Application of this modified log-law is in good agreement with analytical solutions, proposed in previous study to predict the transversal velocity profile. The benefit of this improved modified log-law is its easier practical applicability, i.e., it avoids the measurements of some sensitive turbulence parameters, in addition, the flow hydrodynamic characteristics (U_2, U_m, y_m and δ_2) forming it are predictable, using the initial hydraulic conditions.

Acknowledgement

This study was carried out at the Coastal Engineering Laboratory (L.I.C) of the Technical University of Bari, Italy, Department of Civil, Environmental, Building Engineering and Chemistry.

References

Ben Meftah, M., De Serio, F., Mossa, M., Pollio, A., 2007. Analysis of the velocity field in a large rectangular channel with lateral shockwave. Environ. Fluid Mech. 7 (6), 519–536. http://dx.doi.org/10.1007/s10652-007-9034-7.

Ben Meftah, M., De Serio, F., Mossa, M., Pollio, A., 2008. Experimental study of recirculating flows generated by lateral shock waves in very large channels. Environ. Fluid Mech. 8 (6), 215–238. http://dx.doi.org/10.1007/s10652-008-9057-8.

Ben Meftah, M., Mossa, M., Pollio, A., 2010. Considerations on shock wave/boundary layer interaction in undular hydraulic jumps in horizontal channels with a very high aspect ratio. Eur. J. Mech. – B/Fluids 29, 415–429. http://dx.doi.org/10.1016/j.euromechflu.2010.07.002.

Ben Meftah, M., Mossa, M., 2013. Prediction of channel flow characteristics through square arrays of emergent cylinders. Phys. Fluids 25 (4), 1–21. http://dx.doi.org/10.1063/1.4802047, 045102.

Ben Meftah, M., De Serio, F., Mossa, M., 2014. Hydrodynamic behavior in the outer shear layer of partly obstructed open channels. Phys. Fluids 26 (6), 1–19. http://dx.doi.org/10.1063/1.4881425, 065102.

Ben Meftah, M., De Serio, F., Malcangio, D., Mossa, M., Petrillo, A.F., 2015. Experimental study of a vertical jet in a vegetated crossflow. J. Environ. Manage. 164, 19–31. http://dx.doi.org/10.1016/j.jenvman.2015.08.035.

Ben Meftah, M., Mossa, M., 2016. A modified log-law of flow velocity distribution in partly obstructed open channels. Environ. Fluid Mech. 16 (2), 453–479. http://dx.doi.org/10.1007/s10652-015-9439-7.

Chen, G., Huai, W., Han, J., Zhao, M., 2010. Flow structure in partially vegetated rectangular channels. J. Hydrodyn. 22 (4), 590–597. http://dx.doi.org/10.1016/S1001-6058(09)60092-5.

Helmiö, T., 2004. Flow resistance due to lateral momentum transfer in partially vegetated rivers. Water Resour. Res. 40 (5), 1–10. http://dx.doi.org/10.1029/2004WR003058, W05206.

Hsieh, P.C., Shiu, Y.S., 2006. Analytical solutions for water flow passing over a vegetal area. Adv. Water Resour. 29 (9), 1257–1266. http://dx.doi.org/10.1016/j.advwatres.2005.10.004.

Huai, W., Geng, C., Zeng, Y., Yang, Z., 2011. Analytical solutions for transverse distributions of stream-wise velocity in turbulent flow in rectangular channel with partial vegetation. Appl. Math. Mech. Engl. Ed. 32 (4), 459–468. http://dx.doi.org/10.1007/s10483-011-1430-6.

Huai, W., Xue, W., Qian, Z., 2015. Large-eddy simulation of turbulent rectangular open-channel flow with an emergent rigid vegetation patch. Adv. Water Resour. 80, 30–42. http://dx.doi.org/10.1016/j.advwatres.2015.03.006.

Järvelä, J., 2005. Effect of submerged flexible vegetation on flow structure and resistance. J. Hydrol. 307, 233–241. http://dx.doi.org/10.1016/j.jhydrol.2004.10.013.

Lima, A.C., Izumi, N., 2014. On the nonlinear development of shear layers in partially vegetated channels. Phys. Fluids 26 (8), 1–22. http://dx.doi.org/10.1063/1.4893676, 084109.

Manes, C., Poggi, D., Ridolfi, L., 2011. Turbulent boundary layers over permeable walls: scaling and near-wall structure. J. Fluid Mech. 687 (11), 141–170. http://dx.doi.org/10.1017/jfm.2011.329.

Naot, D., Nezu, I., Nakagawa, H., 1996. Hydrodynamic behavior of partly vegetated open channels. J. Hydraul. Eng. 122 (11), 625–633, ISSN 0733-9429/96/0011-0625-0633.

Nezu, I., Onitsuka, K., 2001. Turbulent structures in partly vegetated open-channel flows with LDA and PIV measurements. J. Hydraul. Res. 39 (6), 629–642. http://dx.doi.org/10.1080/00221686.2001.9628292.

Nikuradse, J., 1933. Strömungsgesetze in rauhen Rohren. Forschungsheft 361. Ausgabe B. Band 4.

Righetti, M., Armanini, A., 2002. Flow resistance in open channel flows with sparsely distributed bushes. J. Hydrol. 269, 55–64, PII: S0 02 2-1 69 4 (0 2) 00 1 94-4.

Rominger, J.T., Nepf, H.M., 2011. Flow adjustment and interior flow associated with a rectangular porous obstruction. J. Fluid Mech. 680, 636–659. http://dx.doi.org/10.1017/jfm.2011.199.

Schlichting, H., 1955. Boundary Layer Theory. Pergamon Press, New York.

Shiono, K., Knight, D.W., 1991. Turbulent open-channel flows with variable depth across the channel. J. Fluid Mech. 222, 617–646. http://dx.doi.org/10.1017/S0022112091001246.

Stephan, U., Gutknecht, D., 2002. Hydraulic resistance of submerged flexible vegetation. J. Hydrol. 269, 27–43. http://dx.doi.org/10.1016/S0022-1694(02)00192-0.

Van Prooijen, B.C., Battjes, J.A., Uijttewaal, W.S.J., 2005. Momentum exchange in straight uniform compound channel flow. J. Hydraul. Eng. 131, 175–183. http://dx.doi.org/10.1061/(ASCE)0733-9429(2005) 131:3(175).

Vermaas, D.A., Uijttewaal, W.S.J., Hoitink, A.J.F., 2011. Lateral transfer of streamwise momentum caused by a roughness transition across a shallow channel. Water Resour. Res. 47 (W02530), 1–12. http://dx.doi.org/10.1029/2010WR010138.

Wang, W., Huai, W., Gao, M., 2014. Numerical investigation of flow through vegetated multi-stage compound channel. J. Hydrodyn. 26 (3), 467–473. http://dx.doi.org/10.1016/S1001-6058(14)60053-6.

White, B.L., Nepf, H.M., 2007. Shear instability and coherent structures in shallow flow adjacent to a porous layer. J. Fluid Mech. 593 (12), 1–32. http://dx.doi.org/10.1017/S0022112007008415.

White, B.L., Nepf, H.M., 2008. A vortex-based model of velocity and shear stress in a partially vegetated shallow channel. Water Resour. Res. 44 (1), 1–15. http://dx.doi.org/10.1029/2006WR005651, W01412.

Xiaohui, S., Li, C.W., 2002. Large eddy simulation of free surface turbulent flow in partly vegetated open channels. Int. J. Numer. Meth. Fluids 39, 919–937. http://dx.doi.org/10.1002/fld.352.

Yang, J.Q., Kerger, F., Nepf, H.M., 2015. Estimation of the bed shear stress in vegetated and bare channels with smooth beds. Water Resour. Res. 51 (5), 3647–3663. http://dx.doi.org/10.1002/2014WR016042.